MASTER THESIS

Development of a blood-retina barrier on-a-chip with human iPSC-derived retinal pigment epithelium and endothelium

Denise Marrero Feitosa-Afonsso

Faculty of Science and Technology
Dr. Andries van der Meer

EXAMINATION COMMITTEE
Prof. Dr. Robert Passier
Dr. Loes Segerink
Daily Supervisor: Yusuf Arik and Giuliana Gagliardi

October 2019

UNIVERSITY OF TWENTE.

Abstract

Age-related macular degeneration (AMD) is a complex and multifactorial disease that causes irreversible central vision loss in the elderly, affecting 170 million people worldwide. The key tissue implicated in the disease is the outer blood-retina barrier (oBRB) composed of the retinal pigment epithelium (RPE), Bruch's membrane, and the choriocapillaris. Despite its high prevalence, the exact cause and onset of the disease remain largely unknown. This is mainly due to the inability of current models to recapitulate the multilayered architecture of the oBRB and capture relevant differences in genetic and environmental variability amongst patients. Therefore, the aim of this research project is to develop a physiologically relevant oBRB-on-a-chip model by mimicking the microenvironment of the RPE-choroid interface *in vitro* with stem cell-derived material. The oBRB architecture was emulated with a co-culture of hiPSC-derived RPE seeded on an open-top chamber interfaced with hiPSC-derived endothelial cells (ECs) embedded into a collagen patterned microchannel. The two generated hiPSC-derived cell types displayed characteristic features of mature and functional cells such as polarized VEGF secretion and angiogenic potential by the RPE and ECs, respectively. Moreover, the ECs in co-culture with the RPE cells expressed the vascular endothelial cadherin marker after three days of culture. This work demonstrates that the co-culture of hiPSC-derived RPE and ECs is compatible with OoC technology and establishes a model for future study of *in vitro* cellular and molecular mechanisms of the RPE-choroid interface.

Contents

List of abbreviations

2D	Two-dimensional space
3D	Three-dimensional space
AMD	Age-related macular degeneration
bFGF	Basic fibroblast growth factor
BrM	Bruch membrane
CA4	Carbonic anhydrase 4
CC	Choriocapillaris
CNV	Choroidal neovascularization
ECM	Extracellular matrix
ECs	Endothelial cells
FITC	Fluorescein Isothiocyanate
GA	Geographic atrophy
hiPSCs	Human induced pluripotent stem cells
HUVEC	Human umbilical vein endothelial cell
MACS	Magnetic-activated cell sorting
MERTK	MER receptor tyrosine kinase
MITF	Melanocyte inducing transcription factor
oBRB	Outer blood-retina barrier
OoC	Organ-on-a-chip
PEDF	Pigment epithelium derived factor
PVLAP	Plasmalemma vesicle associated protein
RPE	Retinal pigment epithelium
RPE65	Retinoid isomerohydrolase RPE65
RT-qPCR	Real time quantitative polymerase chain reaction
SERPINF1	Serpin family F member 1
VEGF	Vascular endothelial grow factor
vWF	Von Willebrand factor
ZO-1	Zona occludens 1

Introduction

Age-related macular degeneration

Age-related macular degeneration (AMD) is a progressive eye disease and the primary cause of irreversible vision loss in the elderly. It affects 170 million people worldwide with a prevalence of one in four over the age of 80 [1,2]. This ocular condition is characterized by vision loss in the center of the visual field preventing patients from performing simple everyday tasks such as recognizing faces, reading, and driving (**Figure 1**). The cause and progression of AMD are complex and multifactorial with genetic and environmental factors playing a role in the pathology, although the exact cause and onset of the disease remain largely unknown. There are two types of AMD, the dry and wet form. Dry AMD accounts for the 85% of the cases and is characterized by the accumulation of insoluble extracellular aggregates of proteins and lipids under the retina, called "drusen"[3]. In later stages, it progresses into geographic atrophy (GA), where there is a substantial cellular death of retinal cells leading to loss of vision. In contrast, the wet form only affects 15% of AMD patients but is responsible for most of the cases of AMD-related blindness[4]. This form is characterized by choroidal neovascularization (CNV), in which blood vessels grow and breach the tissue barriers of the outer retina from the underlying choroid. To date, there is no cure available to remediate the dry form of AMD. However, there are some treatments strategies for the wet form, which are aimed at reducing vessel ingrowth by regular intravitreal administration of α-vascular endothelial growth factor (VEGF) antibodies[5].

Figure 1. *Normal vision (left) and vision of a person with AMD (right).*

The ocular structures implicated in the disease are the retinal pigment epithelium (RPE), Bruch's membrane (BrM), and the choriocapillaris (CC), which altogether compose the outer blood-retina barrier (oBRB) (**Figure 2**). This highly metabolic tissue regulates transport of nutrients and metabolic waste across the barrier. The RPE is a single pigmented monolayer of polarized hexagonal cells with its apical side facing the photoreceptors and its basolateral domain sitting on the BrM. Also, RPE cells provide a physical barrier mediated by tight junction complexes and give metabolic support to photoreceptors by phagocyting the distal part of shed photoreceptor outer segments. Another crucial function of RPE cells is the polarized secretion of growth factors and hormones to ensure tissue homeostasis. Of particular interest is the basolateral secretion of VEGF that supports the maintenance of the adjacent choroidal capillary bed[6]. The CC are composed mostly of endothelial cells (ECs) and are responsible for providing the metabolic needs of the retina. In the healthy retina, the CC lack tight

junctions and are highly fenestrated, forming a dense sinusoidal network with lumens ranging between 20 and 50 µm in diameter[7]. The BrM is a pentalaminar collagen-rich extracellular matrix (ECM) acting as a physical barrier between the RPE and the CC and as a semi-permeable filter regulating the transport of trophic factors[8].

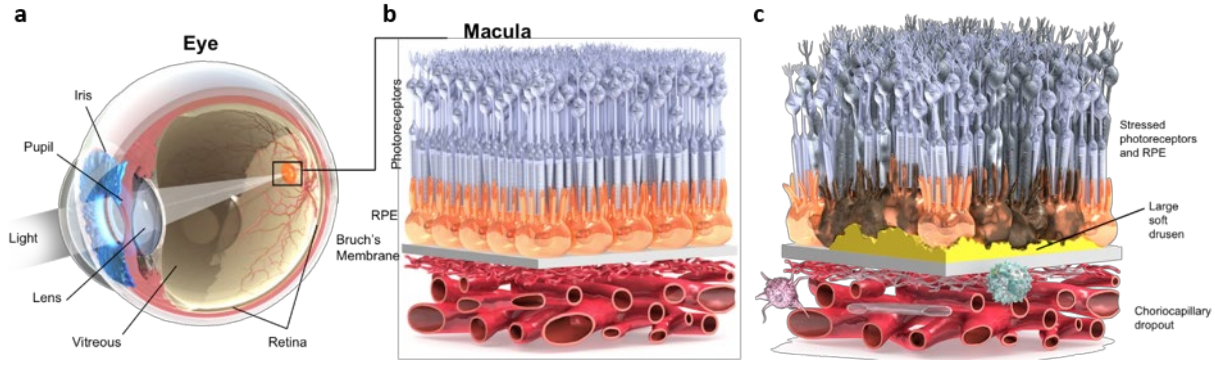

***Figure 2*. Ocular anatomy relevant to AMD**[36]. **a** Cross-section of the eye. **b** Schematic representation of the macular. **c** Schematic representation of the macula in early stages of AMD showing drusen deposits.

In AMD patients, the homeostasis of the oBRB becomes dysregulated, and structural changes in these tissues occur. The pathophysiology mainly affects the macula, a photoreceptor-dense region of the central retina in charge of acuity and central vision. Although the exact molecular mechanisms of the disease remain to be elucidated, the leading events are the dysfunction between the RPE and the underlying CC[9,10]. In the early stages of the disease, there is a decreased density and narrowing of the CC and thickening of the BrM occurs. These events hamper and reduce fluid and nutrient transport across the barrier. Also, drusen accumulation between the RPE cells and the BrM may be indicative of the development of the disease[11]. In the late stages, there is a deterioration of the barrier integrity of the oBRB, which impairs visual performance and can ultimately cause vision loss. In order to elucidate the disease mechanisms of AMD and to develop effective treatments, experimental models that accurately mimic the *in vivo* microenvironment are required.

Current models for AMD

Several *in vivo* and *in vitro* models have been developed to better understand the underlying mechanisms of the disease. However, these models suffer from specific issues in terms of physiology, genetics, anatomy, etc. For instance, physiologically non-human primates have similar characteristics to humans since they possess a macula, but ethical concerns, cost, and prolonged time needed for the disease to develop have restricted their usage[12]. Surprisingly, even though rodents do not possess macula, they are commonly used as models for retinal diseases due to their convenience in housing and breeding, short lifespan, and ease in genetic manipulation[5]. The most common is the laser-induced neovascularization model which is used to examine the formation of new blood vessels of the CC, replicating the main characteristics of CNV[13]. On the other hand, standard cell cultures methods are also used to investigate disease mechanisms of AMD, where experimental conditions can be controlled, and results are more reproducible compared to animal models. However, such systems are typically 2D monocultures which are not capable of replicating tissue-level physiology and function found *in vivo*, such as cell-to-cell and cell-to-ECM spatial interactions or cell polarity.

Over the past decades, different cell sources have been used to study disease mechanisms and identify new drug targets. Immortalized cell lines are widely used because of their unlimited availability, ease of use, and reproducibility. Among the most employed immortalized cell lines to model RPE function and pathology *in vitro* are ARPE-19 and hTERT RPE. Despite their frequent use, these cells possess an altered gene and protein expression, lack pigmentation, and typical cobblestone morphology in standard culture conditions. For EC research, human umbilical vein ECs (HUVECs) have been the "gold standard" due to their ease of access from umbilical cord surplus. However, HUVECs are not representative of the *in vivo* situation because they show significant phenotypic and functional differences from the adult vascular endothelium. Alternatively, adult primary cells obtained directly from postmortem tissues more closely reflect the properties of human tissues and have the highest clinical relevance. This cell source is affected by various limitations such as low availability as only small quantities are normally obtained, complex culture conditions, and time-consuming isolation procedures. Besides, genetic variability is introduced when cells cannot be harvested from the same donor.

The advent of human induced pluripotent stem cells (hiPSCs) provided a cell source free from ethical issues and it enabled the generation of patient-specific material, capturing relevant differences in genetic and environmental diversity. Somatic cells can be harvested from patients by minimally invasive procedures, reprogrammed to a pluripotent state, and then differentiated into any cell type of the human body[14]. The most significant advantage of hiPSCs is that cells generated from AMD patients can be compared to age- or gender-matched control lines, and isogenic lines can be engineered to study the effect of a specific gene mutation. In fact, a study demonstrated that hiPSCs-derived RPE *in vitro* cultures from patients suffering from a specific form of macular degeneration exhibited a larger number of extracellular lipid- and protein-rich deposits compared to control groups[11]. However, their main limitation is that they display an immature phenotype and its low passage number before cellular senescence occurs.

In recent years, organ-on-a-chip (OoC) technology has proven to be a promising alternative to animal use for disease modeling and to develop models in accordance with the *in vivo* milieu. OoCs are microfluidic devices for culturing cells in a controlled microenvironment with the purpose to model functional units of an organ[14]. With this technology, 3D architectures, ECM embedding, vasculature incorporation, and biomechanical cues can be implemented, providing a more realistic model of the human anatomy and function[14]. In addition, OoCs enable the integration of multiple cell types, which are indispensable for the understanding of complex diseases and allow real-time monitoring of biological events that are otherwise not possible in animal models or patients[15,16]. Particularly, relevant oBRB-on-a-chip models that recapitulate organ-level physiology and allow the study of cellular and molecular mechanisms *in vitro* will deliver new insights into the origin and development of AMD, eventually leading to better treatment therapies.

State of the art of outer blood-retina barrier on-a-chip models

So far, there have been three published *in vitro* models of the retina on OoC models summarized in Table 1. The model that was developed by L. Chen *et al.* consists of ARPE-19 and HUVEC monolayers grown on each side of a synthetic porous membrane, cultured in separate microfluidic channels (**Figure 3a**)[17]. Both monolayers are under perfusion, which resembles ECs microenvironment *in vivo* but is not physiological for RPE. Although they claim they could maintain the co-culture for a long time, their results indicated that it was not stable for more than 28 hours. Moreover, the ARPE-19 did not exhibit

characteristic RPE cobblestone morphology nor pigmentation, indicative of the poor physiological relevance of this immortalized cell line.

A more physiologically relevant model is the oBRB on-a-chip representation of M. Chung *et al.* (**Figure 3b**)[18]. The model consists of a static tri-culture of HUVEC, lung fibroblasts, and ARPE-19 where the ECs are embedded into a fibrin scaffold allowing them to generate perfusable 3D blood vessel networks with fibroblasts supporting this network. Between the EC compartment and the RPE monolayer, there is a 300 µm gap made of fibrin acting as an interstitial ECM to avoid the spontaneous invasion of the ECs towards the RPE and as a window to study vessel ingrowth. This 300 µm gap reduces the physiological relevance of the model in terms of permeability and transport since the BrM has a thickness of 4 µm[8]. Also, to assess the barrier integrity of the model they used a 10 kDa FITC-Dextran molecule. Their results demonstrated that the RPE-choroid complex was leak-tight for that specific fluorescent dye. Nevertheless, the molecular weight of the VEGF monomer is 21 kDa which prevents the study of the crosstalk between the RPE and the CC.

The latest publication of the oBRB on-a-chip model by J. Peak *et al.* consists of an open-top chamber for epithelial cell culturing located above a compartment for the formation of 3D vascular networks (**Figure 3c**) [19]. This compartment is flanked by two parallel microchannels by which media was supplied and each channel was connected to a syringe pump. In contrast to the previous models, the cells used for this model were primary human retinal microvascular ECs, primary human ocular choroid fibroblasts, and hiPSC-derived RPE cells. Interestingly, their results prove a positive synergistic effect of the tri-culture. For example, the laminin deposition by the RPE monolayer was doubled and the number of melanosomes increased by 3-fold when cultured together with the vasculature. One confounding factor is the absence of any membrane between the vasculature and the RPE since the BrM is very important to capture the structural complexity of the oBRB; as was observed in the previous model, a 300 µm gap was needed to avoid the invasion of the ECs towards the RPE monolayer. Lastly, the tri-culture was maintained in culture for 14 days which is a limitation for the study of prolonged molecular processes, *e.g.,* extracellular deposits by RPE cells on the BrM[11].

Table 1. *Overview of the different oBRB models on-a-chip*

	Cell source	Surface properties	ECM interactions	Biological triggers	Mechanical cues	Read-outs
L. Chen, et al. (2017)	ARPE-19 (2D) & HUVEC (2D)	6.5 µm-thick membrane with 10 µm pore size	Fibronectin coating	Glucose and hypoxia	Shear stress by a syringe pump	Immunohistochemistry (TJs), permeability assay (70 kDa), VEGF secretion
M. Chung, et al. (2018)	ARPE-19, HUVEC, & fibroblast	Fibrin hydrogel on microposts array	Fibrin scaffold	VEGF exposure & bevacizumab treatment	Static culture	Immunohistochemistry (TJs, laminin, & collagen IV), permeability assay (10 kDa), VEGF & PEDF secretion
J. Paek, et al. (2019)	Retinal microvascular ECs, fibroblast, & hiPSC-RPE	Membrane-free	Fibrin & collagen I scaffold	-	Shear stress by a syringe pump	Immunohistochemistry (CD31, TJs & laminin), Permeability assay (70 kDa),

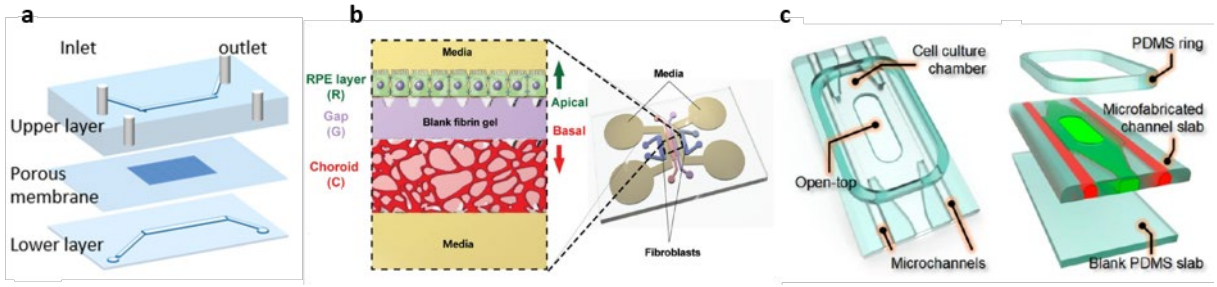

Figure 3. **Schematic representation of the existing microfluidic devices to mimic the oBRB**. **a** Design of the 2D culture of HUVEC and ARPE-19 model developed by L. Chung *et al.*[17] **b** Schematic representation of the tri-culture model of the RPE-choroid interface developed by M. Chung *et al.*[18] **c** 3D cell culture platform generating perusable vasculature networks and an open top chamber for epithelial cell culturing developed by J. Peak *et al*. [19]

Aim of the project

The goal of this research project was to develop a physiologically relevant oBRB-on-a-chip model by mimicking the microenvironment of the RPE-choroid interface *in vitro*. More specifically, the purpose was to improve the current oBRB model developed at the University of Twente, by incorporating RPE and ECs derived from hiPSC control lines. The first half of the project was dedicated to generating and characterizing hiPSC-derived RPE and ECs. Differentiation and maturation of hiPSC-derived cells were assessed by immunostaining and RT-qPCR of RPE and EC specific markers, respectively. The second part of the project consisted of incorporating the two generated hiPSC-derived cells types into the OoC device. First, each cell type was characterized and optimized as a monoculture on the microfluidic device. Then, co-culture of hiPSC-derived RPE and ECs was developed to complete the oBRB-on-a-chip model. This work demonstrates that the co-culture of hiPSC-derived RPE and ECs is compatible with OoC technology and establishes a model for future study of *in vitro* cellular and molecular mechanisms of the RPE-choroid interface.

This project was carried out in collaboration between the department of Applied Stem Cell Technologies at the University of Twente and the department of ophthalmology at Radboud University Medical Center in Nijmegen.

Materials and methods

Differentiation and maintenance of hiPSC-derived RPE

The protocol used to differentiate hiPSCs into RPE has been based on the protocol developed by Reichman *et al.* with some modifications[20]. Undifferentiated hiPSCs were expanded to 70-80% confluence on 6-cm diameter dishes coated with matrigel growth factor reduced (CORNING) in essential 8 medium (Thermo Fisher Scientific). At this time point (D_0) hiPSCs were cultured in essential 6 medium (Thermo Fisher Scientific). After 2 days (D_2), the medium was replaced for E6N2 composed of essential 6 medium supplemented with 1% N2 supplements (Thermo Fisher Scientific), and 0,2% primocin (Invivogen). On day 28 (D_{28}), the medium was switched to FMN composed of DMEMF:Nutriend Mixture F-12 (DMEM/F12, 1:1, L-Glutamine, Thermo Fisher Scientific) and supplemented with 1% N2 supplements, 1% non-essential amino acids (MEM-NEAA; Sigma-Aldrich), and 0,2% primocin. The medium was changed once every 2-3 days.

Around day 42, pigmented patches of hiPSC-derived RPE were manually isolated and transferred onto plates coated with truncated recombinant human vitronectin (rhVTN-N; ThermoFisher) diluted in phosphate buffered saline (PBS). At this time point, hiPSC-derived RPE cells were labeled as passage 0 (P_0) and were expanded in FMN medium. Once cells reached confluency, hiPSC-derived RPE cells were washed with PBS, dissociated with TrypLE Select (Thermo Fisher Scientific) for 20 min, spinned down at 200 G for 3 min, and replated at $4 \cdot 10^5$ cells/cm^2 in T-25 cm^2 rhVTN-N-coated flask for amplification. The medium was refreshed once every 2-3 days.

Differentiation and maintenance of hiPSC-derived ECs

The protocol used to differentiate hiPSCs into ECs has been based on the protocol developed by Orlova *et al.* with some modifications[21]. Undifferentiated hiPSCs were expanded to 10 to 20% confluence on a 6-well plate coated with matrigel - growth factor reduced in essential 8 medium. At this time point (D_0) hiPSCs were stimulated to a mesoderm lineage by culturing in BPEL medium (described below) and 8 µM of CHIR99021 (Tocris). At day 3 (D_3), medium was switched to BPEL with 50 ng/mL VEGF165 (Peprotech) and 10 µM of SB-431542 (Stemgent) for vascular specification. At day 10 of differentiation, cells were analyzed with flow cytometry and CD31-positive cells were magnetically sorted.

After CD31-based MACS, hiPSC-derived ECs labeled as passage 0 (P_0) were transferred to 0.1% gelatin coated 6-well culture plates and cultured in EC-SFM medium composed of human endothelial serum-free medium (Thermo Fisher Scientific), 1% of platelet-poor plasma-derived human serum (Sigma-Aldrich), 30 ng/ml of VEGF (Peprotech), and 20 ng/ml of bFGF (Stemcell Technologies) for amplification. Upon confluence, cells were washed with PBS, detached with TrypLE Select, pelleted at 300 G for 3 min, and replated at $1.5 \cdot 10^5$ cells/cm^2 in a T-75 cm^2. The medium was changed once every 2-3 days.

BPEL preparation

For the differentiation of hiPSC-derived ECs, BPEL was prepared with 44.45% of Iscove's Modified Dulbecco's Medium (IMDM; Termo Fisher Scientific), 44.45% of Ham's F-12 Nutrient Mixture (F-12; Termo Fisher Scientific), 5% Protein Free Hybridoma Medium II (PFHM II; Termo Fisher Scientific), 2,5% of Bovine Serum Albumin (BSA; Sigma-Aldrich) in IMDM medium, and supplemented with 1% of Chemically Defined Lipid Concentrate (Termo Fisher Scientific), 1% of L-Ascorbic acid 2-phosphate

sesquimagnesium salt hydrate (Sigma-Aldrich), 1% of GlutaMAX™ Supplement, 0.1% of Insulin,-Transferrin-Selenium-Ethanolamine (ITS-X; Termo Fisher Scientific), 0.3% of α-Thioglycerol (Sigma-Aldrich), and 0.2% of primocin (InvivoGen). The medium was stored at +4°C and used within 2 weeks.

Magnetic-activated cell sorting (MACS)

Cells were washed with PBS and disaggregated from the cell culture plates by incubation with TrypLE Select for 6-8 min at RT and pelleted at 300 G for 3 min. Cells were resuspended in MACS buffer composed of 0,5% BSA, 2 mM of EDTA in PBS. Then, cells were passed through a 30-µm strainer (Miltenyi Biotec) to achieve a single cell suspension. Dissociated cells were incubated with CD31 antibody (1:10, Miltenyi Biotec) in the dark at 4°C for 10 min. After washing with MACS buffer, cells were incubated with α-mouse IgG1 MicroBeads (1:5, Miltenyi Biotec) in the dark at 4°C for 15 min. Cells were resuspended in 500 µL of MACS buffer and applied onto a MS positive selection column fixed to a MACS separator. The flow-through containing the CD31-population was collected in a tube followed by 3 x 500 µL washes with MACS buffer. The CD31-positive population retained in the column was eluted with 1 mL of MACS buffer after magnet removal from the MACS separator. To assess the efficiency of MACS, $2 \cdot 10^5$ cells of the CD31-positive and CD31-negative population were labeled with VE-cadherin-488 (1:50) antibody in the dark at 4 °C for 10 min. Cells were washed once and resuspended in 300 µL for flow cytometry analysis.

Flow cytometry

Cells were washed with PBS and disaggregated from the cell culture plates by incubation with TrypLE Select for 6 to 8 min at room temperature (RT). Cells were neutralized by adding MACS buffer and large particles were removed with a 30-µm strainer (Miltenyi Biotec). Approximately $2 \cdot 10^5$ cells were suspended in 100 µL MACS buffer and labeled with CD31-APC (1:100; Miltenyi Biotec), VE-cadherin-488 (1:50; Miltenyi Biotec), and appropriate APC (1:100; Miltenyi Biotec) and Alexa Fluor 488 (1:100; Thermo Fisher Scientific) isotype controls antibodies in the dark at 4 °C for 10 min. Cells were washed once with PBS and resuspended in 300 µL in MACS buffer. For analysis, forward and side scatter gate was set to exclude dead cells and aggregates and a minimum of 10^4 events in the live cell gate were collected. Background fluorescence and non-specific binding were measured using unstained cells and isotypic control, respectively. Analysis was performed with Gallios flow cytometer (Beckman Coulter) and data were analyzed with Kaluza software (Beckman Coulter).

Immunohistochemistry

Cells cultured in slide flasks or glass cover slips, were first washed twice in PBS, and then fixed at 4°C for 10 min using 4% paraformaldehyde. After fixation, cells were washed for 5 min with PBS. Next, cells were permeabilized for 5 min with 1% Triton X-100 (Sigma-Aldrich) in PBS and blocked for 20 min with blocking buffer (2% BSA in PBS). The slide flasks or the cover slips were incubated with the primary and the secondary antibodies in blocking buffer for 1 h and 45 min, respectively. Afterwards, nuclei were stained with Hoechst (1:1000; Thermo Fisher Scientific) for 15 min. The following primary antibodies were used: rabbit α-ZO-1 (1:200; Thermo Fisher Scientific), mouse α-MITF (1:200; Dako-Agilent), mouse α-CD31 (1:200; Dako-Agilent), rabbit α-VE-cadherin (1:200; Cell Signaling Technology), and rabbit α-Von Willebrand factor (vwF; 1:200; Dako-Agilent). The following secondary antibodies were used: goat α-mouse-488 (1:250; Invitrogen), goat α-rabbit-568 (1:250; Molecular Probes). All steps were performed at RT unless otherwise stated.

Tube formation assay

Matrigel growth factor reduced was thawed overnight at 4°C on ice. 280 µL of 10 mg/mL of Matrigel was distributed into each well of a 24-well culture plate and incubated for 30 to 60 min at 37 °C to allow the gel to polymerize. After that, $4 \cdot 10^5$ cells/well hiPSC-derived EC at passage 1 were seeded onto the gel and cultured for 24 h at 37 °C until image acquisition.

RNA isolation, cDNA synthesis, and RT-qPCR

Total RNA was extracted with lysis buffer and purified using the NucleoSpin® RNA kit (MACHEREY-NAGEL) according to the manufacturer's instructions. RNA yield was determined using the NanoDrop 2000 spectrophotometer (Thermo Scientific). Equal amounts of cDNA were converted to RNA using iScript™ cDNA Synthesis Kit (BIO-RAD). Real Time Quantitative PCR (RT-qPCR) was performed using TaqMan™ Fast Advanced Master Mix (Applied Biosystems) and detection was achieved using the QuantStudio 3 Real-Time PCR System (Thermo Fisher Scientific). Expression of target genes was normalized to reference gene 18S and quantification of gene expression was based on the DeltaCt Method. TaqMan probe assay IDs are listed in Supplementary Table 1.

VEGF release quantification.

Commercially available Human VEGF ELISA Kit (Invitrogen) was used to determine the amount of VEGF secretion from hiPSC-derived RPE following manufacturer's instructions. hiPSC-derived RPE were seeded on Transwell with 0.4 µm pore polyester membrane cell culture inserts (Corning) pre-coated with rhVTN-N. The culture medium was collected at different time points and stored at -80 °C until usage. The fluorescent intensity at 450 nm was measured with the Victor 3 microplate fluorometer (Perkin Elmer).

Device fabrication

Poly(methyl methacrylate) (PMMA) (Altuglass, France) master models were designed with SolidWorks and fabricated with a computer numerical control milling machine (Datron Neo, Datron AG, Germany). The three-layered devices (**Figure 4**) were made by mixing poly(dimethylsiloxane) (PDMS; Dow Corning Sylgard 184) base and curing agent in a 10:1 wt ratio and poured onto their respective micromilled master molds. Next, it was degassed under vacuum pressure to remove bubbles, and cured at 70 °C for at least 3 hours. Following curing, PDMS were removed from the molds and cut into individual chips since each mold generated four chips. The inlet- and outlet holes, the open-top culture chamber, and the reservoirs were punched with 1.25, 3, and 5 mm diameter biopsy punches (Robbins Instruments), respectively. For the device assembly, a PDMS/Toluene mortar (5:3 wt ratio) (Toluene from Merck) was spincoated onto a glass coverslip (1500 rpm, 60s, 1000 rpm/s, Spin150, Polos) and transferred to the PDMS slabs containing the microchannel, the inlet- and outlets and the open-top reservoir using a ink roller. Next, an ~0.36 cm^2 8 µm pore sized polyester membrane (GVS Life Science) was aligned and sandwiched between the center of the microchannel and middle compartments. Finally, the assembled devices were baked at 70 °C overnight. Prior to functionalization, the PDMS layer containing the

reservoirs were attached to the assembled devices by treating both surfaces with air plasma (50W) for 40 seconds (CUTE, Femto Science).

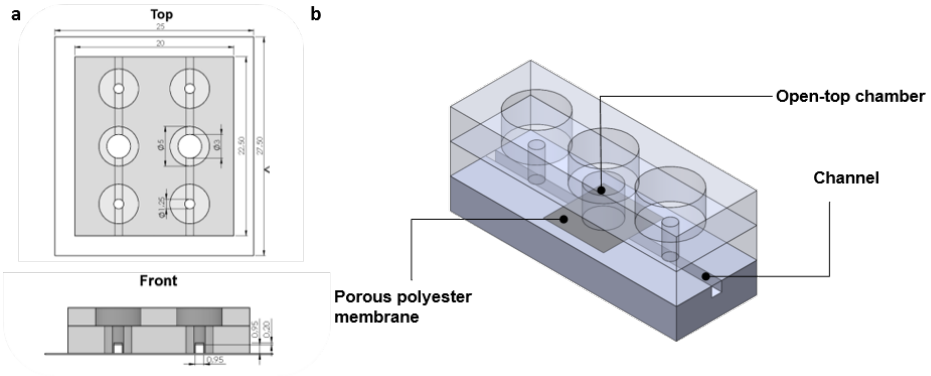

Figure 4. **Three-layered PMDS-based microfluidic device for oBRB modeling. a** The device consist of two independent culture units. Each unit is composed of a bottom compartment with a defined (0,95 mm x 0.95 mm) channel for hiPSC-derived ECs culture and an open-top chamber with diameter of 0.3 mm for hiPSC-derived RPE culture. **b** Overview of a culture unit of the microfluidic device with a polyester membrane with 8 µm pore size and 10 µm thickness separating the channel from the open-top chamber.

Surface modification of PDMS

Following assembly, the microfluidic devices were chemically functionalized for enhancing hydrogel adhesion by using 3-(Aminopropyl)triethoxysolane (APTES; Sigma Aldrich) and glutaraldehyde (Sigma Aldrich). 3% APTES mixed in ultrapure H_2O (ELGA) was added into the channels and open-top chambers and incubated 5 min at RT. The APTES solution was removed by thorough rinsing the devices with 100 % ethanol and subsequently incubated in 100% ethanol in order to remove the remaining APTES. This was followed by blow drying the devices with air. After that, 10% glutaraldehyde (GA, Thermo Fisher) was pipetted into the channels and open-top chambers and the devices were incubated for 5 min at RT. The devices were then washed thoroughly with distilled H_2O (dH_2O) and air dried at 60 °C for at least 2 hours until patterning.

Hydrogel patterning

Before the addition of collagen, the reservoirs were sealed with scotch tape (3M) to avoid collagen flowing to the reservoirs. The devices were kept on ice in order to avoid premature and incomplete collagen gelation in the channels. Rat tail collagen type I (VWR) was prepared according to the manufacturer's instructions at a concentration of 6mg/ml and a pH between 7.5 and 8 by mixing dH_2O, PBS and 1M sodium hydroxide solution. Collagen solution was then pipetted into the channel through one side of the microchannel. Next, two stripped 20G blunt needles (METCAL) were inserted into the side inlets until underneath the inlet holes, and a needle with an outer diameter of 510 µm (SurGuard, VWR) with the cap removed was guided through the blunt needles. The devices were incubated at 37 °C for 60 min for collagen to gelate. Upon hydrogel polymerization, the needles and the wire were carefully removed. Channels were sealed by inserting square polystyrene plugs ($1mm^2$, Evergreen Scale Models). 100 µL of medium was added to the inlets to prevent hydrogel dehydration. After hydrogel polymerization, the devices could be stored at 4°C for up to two weeks.

Microfluidic cell culture

hiPSC-derived RPE culture. Before hiPSC-derived RPE seeding, the open-top chamber was coated with rhVTN-N for 1 h at RT. Then, hiPSC-derived RPE were dissociated according to their protocol mentioned above and resuspended in FMN at a concentration of $2{,}2 \cdot 10^6$ cells/mL. 20 µL of cell suspension was pipetted into the open-top chamber. When hiPSC-derived EC were cultured alone, 60 µL of FMN was added on each of the three reservoirs. Media was replaced once every 2-3 days and cells were used at passage 2.

***hiPSC-derived ECs culture*.** After hydrogel patterning, hiPSC-derived EC were dissociated according to their protocol described above and resuspended in EC-SFM in a concentration of $5 \cdot 10^6$ cells/mL. 10 µL of cell suspension was dispensed into the microchannel inlet. Excess suspension was aspirated from the outlet hole to stop the cells flow in the microchannel. Afterwards, the device was turned upside down in order to seed the ceiling of the microchannel for 1 hour at 37°C and 5% CO_2. After optical confirmation that the cells were attached, 10 µL of cell suspension was loaded into the inlet to seed the bottom of the lumen. When only hiPSC-derived EC were cultured, 60 µL of EC-SFM was added on each of the three reservoirs. Media was replaced once every day and cells were used up to passage 3.

hiPSC-derived RPE and ECs co-culture. After hydrogel patterning, the open-top chamber was coated with rhVTN-N for 1 h at RT. Next, the dissociated hiPSC-derived RPE cells were seeded on the open-top chamber as described above. The cells were allowed to grow into a confluent monolayer until pigmentation was visible around day 17 of on-chip cultures. Then, the hiPSC-derived ECs were seeded as described above into the microchannel inlet. The medium was replaced to complete EC-SFM and was replaced every day.

Statistics and Data Analysis

Images were analyzed with Fiji software. Data analysis was performed using GraphPad Prism 6 (GraphPad Software). Error bars represent the standard deviation.

Results

Generation of hiPSC-derived RPE. The protocol used to differentiate hiPSCs into RPE is based on a spontaneous and 2D adherent culture differentiation method developed by Reichman *et al.* (**Figure 5a**). RPE cells were derived from three control hiPSC lines: ips17-00096, ips17-00095, and ips17-00041. To encourage the spontaneous differentiation of hiPSC colonies, basic fibroblast factor (bFGF) was removed from the medium for two days (**Figure 5b**). From day 2 until day 28, cells were stimulated towards a neuroectoderm lineage with a medium containing a neural supplement. During this process, around day 22 the first neuro-epithelial like structures started to appear around of which RPE grow (**Figure 5c**). Next, to facilitate the maturation and expansion of the RPE, cells were cultured in a retinal maturation medium until pigmented patches were mechanically isolated at day 42 (**Figure 5d**) and transferred onto rhVTN-N-coated plates for expansion. After at least 3 weeks of culture, they formed a confluent monolayer with typical cobblestone morphology and pigmentation (**Figure 5e**).

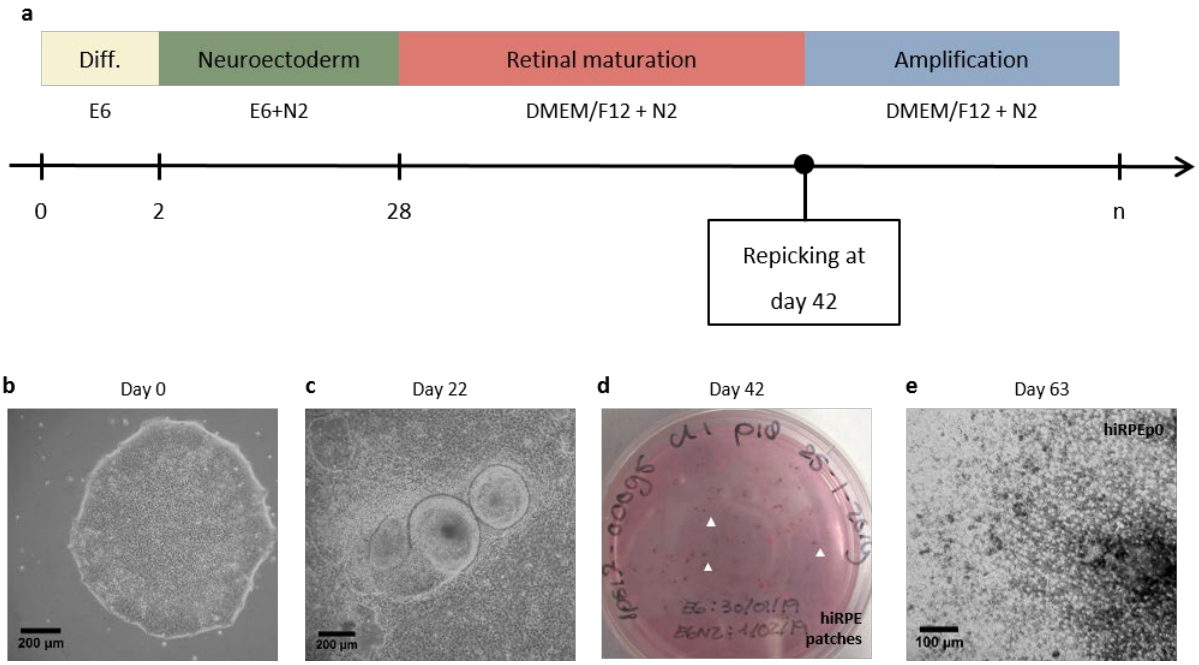

Figure 5. **Differentiation of hiPSC into RPE. a** Timeline of differentiation protocol for the generation of hiPSC-derived RPE. **(b-e)** Brightfield images of hiPSCs at different stages of differentiation. **b** Colony size at the time point of differentiation induction. **c** Emergence of neuroepithelial-like structures around day 22 of differentiation. **d** Pigmented patches of hiRPE cells at day of repicking (D42). Arrow heads indicate some hiRPE pigmented patches. **e** Confluent and pigmented monolayer of hiRPE cells at passage 0 after repicking.

Characterization of hiPSC-derived RPE. The generated hiPSC-derived RPE were capable of expressing differentiation and polarization features characteristic of mature RPE such as EZRIN and BESTROPHIN1, which are expressed in the apical and basolateral side, respectively (**Figure 6a-b**). Also, the hiPSC-derived RPE were immunoreactive to the tight junction protein ZO-1, indicating the presence of a tight cellular barrier. (**Figure 6c**). RT-qPCR analysis also demonstrated that the differentiated cells expressed RPE-specific markers associated with retinoid cycle (*RPE65*), phagocytosis (*MERKT*), eye field specification marker (*MITF*), and secretion of two growth factors (*VEGF* and *PEDF*) (**Figure 6d**). At gene expression level, there were significant differences between the hiPSC-derived RPE and two immortalized cell lines:

ARPE-19 and hTERT RPE. The *RPE65* gene expression was upregulated by 200-fold, highlighting the biological differences between our generated cells and immortalized cell lines. The same trend holds true for the *MITF* and *MERKT* gene expression, which were 5- and 20-fold upregulated, respectively. Interestingly, the expression of the gene encoding for pigment epithelium derived factor (*PEDF)*, a growth factor with antiangiogenic potential, was upregulated 100-fold; whereas the expression of *VEFG* decreased by 2-fold. To quantify the amount of VEGF secreted by the hiPSC-derived RPE, a VEGF ELISA was performed on the basal and the apical domains supernatants. HiPSC-derived RPE secreted VEGF from both the apical and basal sides. As expected, secretion was significantly higher on the basal side from day 17 onwards and cytokine secretion profile reached a plateau overtime. These findings demonstrate that our differentiated hiPSC-derived RPE display characteristic features of mature and functional RPE with polarized secretion of VEGF.

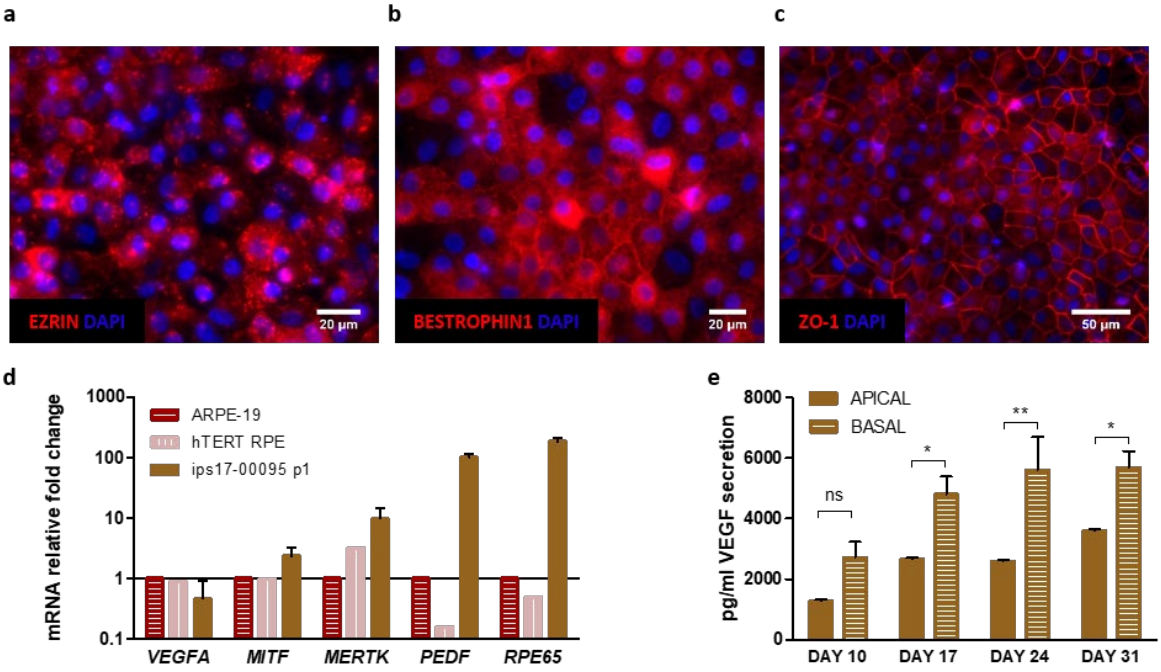

Figure 6. **RPE specific markers expression of hiPSC-derived RPE by immunohistochemistry and RT-qPCR. (a-c)** Maximum projections of microscopic images of EZRIN, ZO-1, and BESTROPHIN1 immunostainings after 3 weeks of hiPSC-derived RPE. **d** Gene expression in hiPSC-derived RPE at passage 1 of cell line ips17-00095. The graph shows data of two biological replicates. Gene expression is indicated relative to ARPE-19 at passage 16. **e** ELISA quantification assay of apical and basal VEGF secretion at different time points of hiPSC-derived RPE grown on Transwell inserts. The graph shows data of two biological replicates. Values represent the mean ± SD.

Generation of hiPSC-derived ECs. The protocol used to differentiate hiPSCs into ECs is based on a 2D adherent protocol developed by Orlova *et al.* ECs were generated from two control hiPSC lines: ips17-00095, and ips17-00041 (**Figure 7a**). To start the differentiation, mesoderm specification was induced by addition of CHIR99021, a small molecule inhibitor of the glycogen synthase kinase-3β pathway. Up to day 3, hiPSC colonies expanded to populate the entire culture dish and mesenchymal cells were observed by their defined borders and polygonal shape (**Figure 7c**). From day 3 onwards, vascular specification was induced by the removal of mesoderm-inductive factors and the addition of VEGF and the transforming growth factor-β (TGF-β) inhibitor SB431512. This molecule is a TGF-β pathway inhibitor that supports ECs expansion. On day 6, the firsts ECs islands could be observed, and they kept expanding until isolation was performed on day 10 (**Figure 7d-e**). As stablished by Orlova *et al*., isolation was

performed on day 10 of the differentiation protocol due to the higher co-expression of VE-cadherin and CD31, two specific endothelial transmembrane proteins crucial for vessel formation.

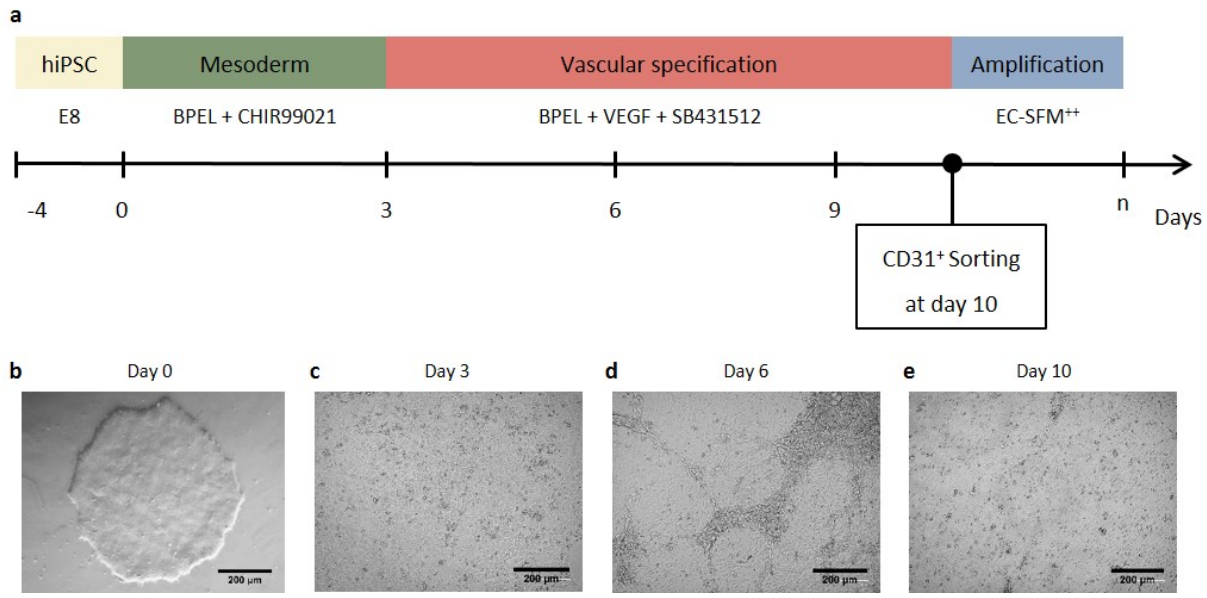

Figure 7. **Differentiation of hiPSC into ECs. a** Timeline of differentiation protocol for the generation of hiPSC-derived ECs. (b-e) Brightfield images of hiPSCs at different stages of differentiation. **b** Colony size at the time point of differentiation induction. **c** Emergence of mesenchymal cells at day 3 of differentiation. **d** Emergence of the first ECs islands at day 6 of differentiation. **e** Expansion of ECs islands until day 10 of differentiation in which they are sorted by the specific surface marker CD31.

Isolation and amplification of hiPSC-derived ECs. To evaluate the ability of the two different hiPSC lines to undergo vascular linage commitment as well as the efficiency of the magnetic sorting, the expression of CD31 and VE-cadherin, were assessed before and after isolation by flow cytometry. **Figure 8a-d** shows a representative flow cytometry analysis for cell line ips17-00095 on day 10 of differentiation. The cell population was examined by side scatter (SS) versus forward scatter (FS) dot plot, which allowed to gate the live population for further analysis (**Figure 8a**). The yield of CD31 and VE-cadherin expression of the differentiated cultures before isolation is represented on **Figure 8b**. The percentage of hiPSC-derived ECs co-expressing CD31 and VE-cadherin surface markers at the end of the differentiation was 16.32% indicating that one sixth of the hiPSCs committed to a vascular lineage. After MACS positive selection for CD31-expressing cells, the percentage of cells co-expressing CD31 and VE-cadherin was enriched up to 96.82 % (**Figure 8c**), whilst the CD31-negative fraction did not express CD31 nor VE-cadherin marker (**Figure 8d**). Flow cytometry performed on day 9 and 11, indicated no statistically significant differences on the CD31 and VE-cadherin co-expression, although it exhibited a tendency to increase over time (**Figure 8e**). Also, the two different hiPSC lines had nearly the same differentiation efficiency of 23,07 ± 5.76 % and 31,61 ± 4.14 % for line ips17-00096 and ips17-00041, respectively (**Figure 8f**).

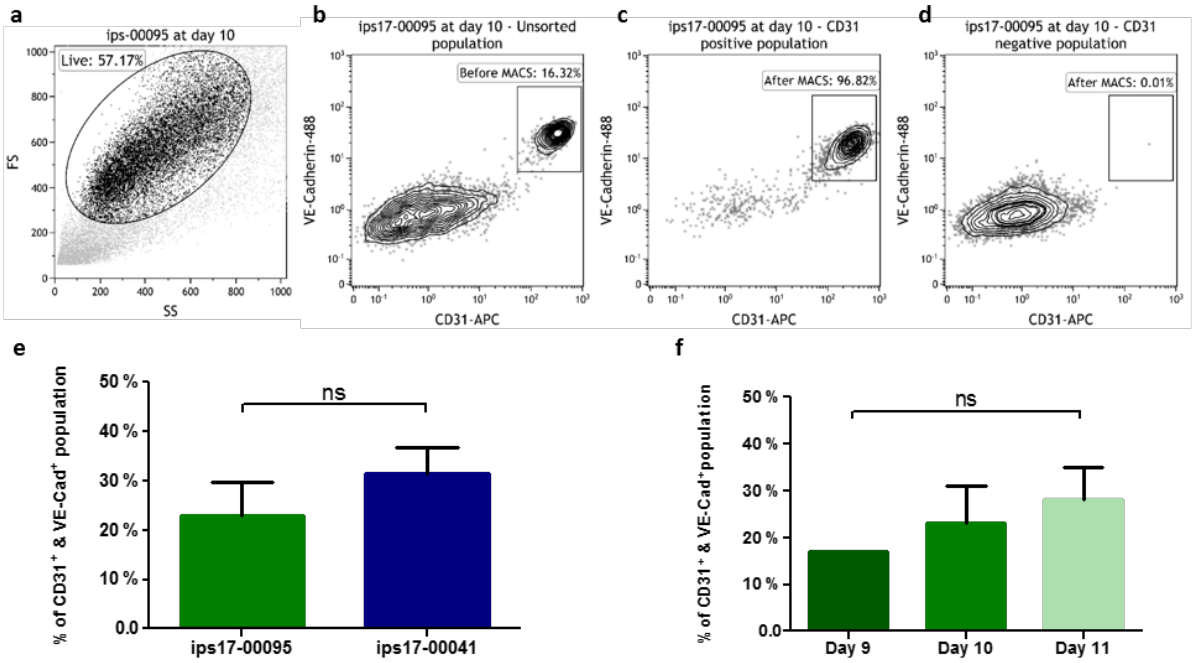

Figure 8. **Flow cytometric analysis of VE-cadherin and CD31 expression of hiPSC line ips17-00095 at day 10 of differentiation.** **a** FS versus SS of unstained sample and gated from live cell population (57,2%). **b** Flow cytometry analysis of VE-cadherin and CD31 surface markers within live gate of unsorted population within live gate of unsorted population, and after MACS **c** within live gate of CD31-positive population, and **d** within live gate of CD31-negative population. **e** Quantification of the percentage of VE-cadherin/CD31-positive cells at day 10 of differentiation of two hiPSC lines. The graph shows the average of differentiation outcomes for line ips17-00095 (n=3) and ips17-00041 (n=4), respectively. Error bars represent ± SD. **f** Differentiation efficiency of line ips17-00095 for days 9, 10, and 11, respectively. The graph shows data od differentiation outcomes for day 9 (n=1), 10 (n=3), and 11 (n=2), respectively.

Characterization of hiPSC-derived ECs. The enriched CD31-positive population displayed typical ECs morphology (**Figure 9a**). Immunofluorescence results further confirmed the co-localized expression of the markers CD31 and VE-cadherin in hiPSC-derived ECs, as well as the expression of the Von Willebrand Factor (vWF), another specific marker of ECs (**Figure 9b-c**). Next, the ability of the cells to form tubes was evaluated, in order to assess the angiogenic potential of the hiPSC-derived ECs *in vitro*. After 24 h from seeding, formation of structures resembling a vascular network were observed (**Figure 9d**). However, when tube formation assay was performed on 6 mg/ml collagen, cells were unable to form tubes within the gel, instead they grew as a monolayer (data not shown). Finally, we evaluated the gene expression of endothelial specific markers in the two different hiPSC lines compared to HUVEC (**Figure 9e**). Both hiPSC-derived EC lines at passage 2 expressed similar mRNA levels of *CD31* and *VE-cadherin*. Interestingly, the mRNA expression of *vWF* was highly upregulated, as well as the expression of two important markers of fenestrated capillaries such as *CA4*, and *PVLAP*. These results demonstrate that the protocol is robust and reproducible, since the two different hiPSC lines show similar differentiation efficiency and gene expression levels, resulting in ECs with angiogenic potential *in vitro*.

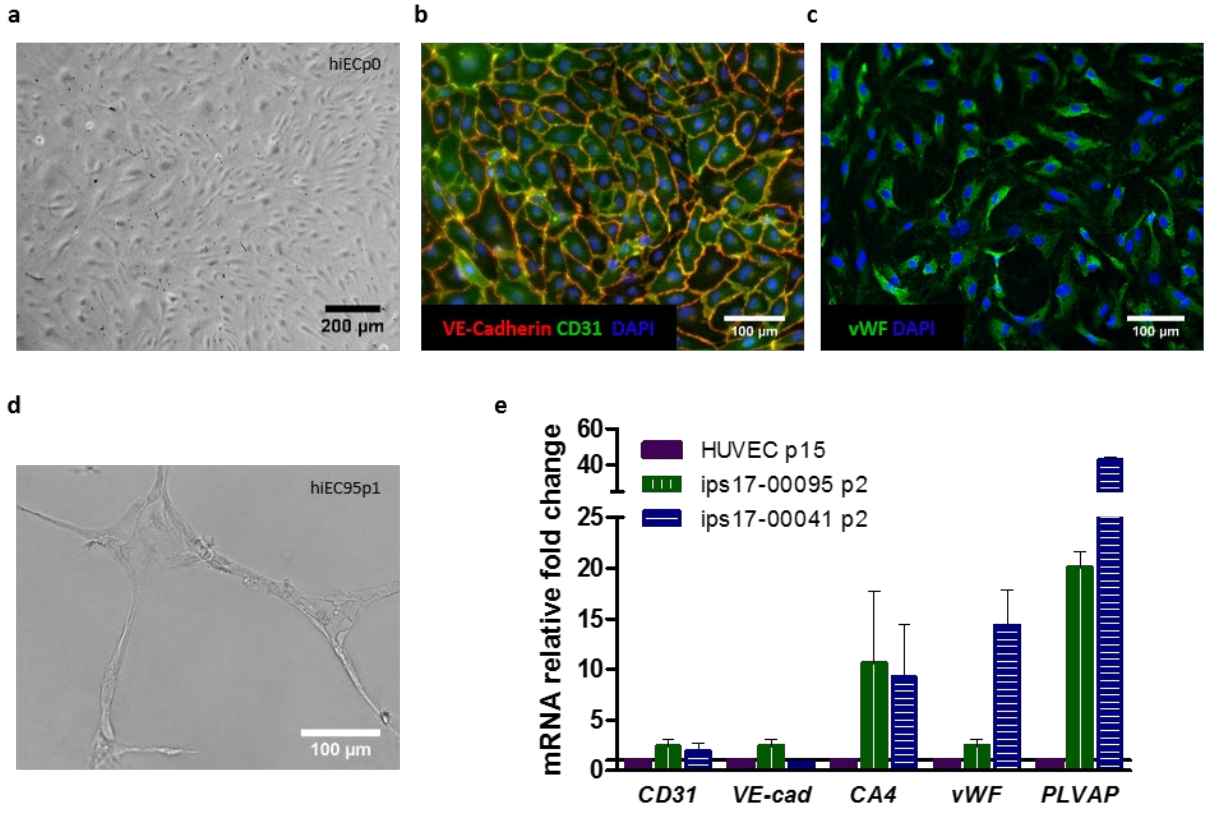

Figure 9. **Characterization of hiPSC-derived EC after isolation. a** Confluent hiPSC-derived EC monolayer at passage 0 after MACS. (**b-c**) Maximum projections of microscopic images of **b** VE-cadherin in red and CD31 in green surface markers and **c** cytoplasmatic vWF in green. **d** Tube formation assay of hiPSC-derived EC at passage 1 and plated on Matrigel for 24 h. **d** Gene expression analysis of hiPSC-derived EC at passage 2 of two cell lines. The graph shows data of three and two biological replicates for line ips17-00095 and ips17-00041, respectively. Data was normalized by 18S and expressed normalized to HUVEC at passage 15. Values represent the mean ± SD.

Culturing of hiPSC-derived ECs on-a-chip. First, to evaluate if the microfluidic device supports the culture of hiPSC-derived ECs and RPE, the two cell types were characterized, and their culture was optimized separately. Each chip consists of a microchannel for culturing hiPSC-derived ECs in intimate contact with an open-top chamber, where hiPSC-derived are seeded on an 8 µm pore size polyester membrane. To generate hollow microchannels collagen type I is used as a hydrogel (**Figure 10a**). Collagen integrity was crucial for tube formation. After hiPSC-derived ECs seeding in the collagen-patterned microchannel, cells start to proliferate and line the surface of the channel until they form a confluent monolayer (**Figure 10b**). The culture remained viable up to ten days (data not shown). The actin staining confirmed that the hiPSC-derived ECs formed a continuous monolayer covering the perimeter of the patterned collagen hydrogel (**Figure 10c**). **Figure 10d** shows a 3D reconstruction fluorescent image of the tube formed by hiPSC-derived ECs grown directly against the collagen where the tubule had a clear lumen. hiPSC-derived ECs cultured in a 3D environment exhibited a different mRNA expression profile compared to cells grown as a monolayer. As expected, the expression of EC-specific markers was up-regulated when grown on a 3D configuration corroborating the relevance of culturing cells in a more complex environment, more representative of the *in vivo* situation.

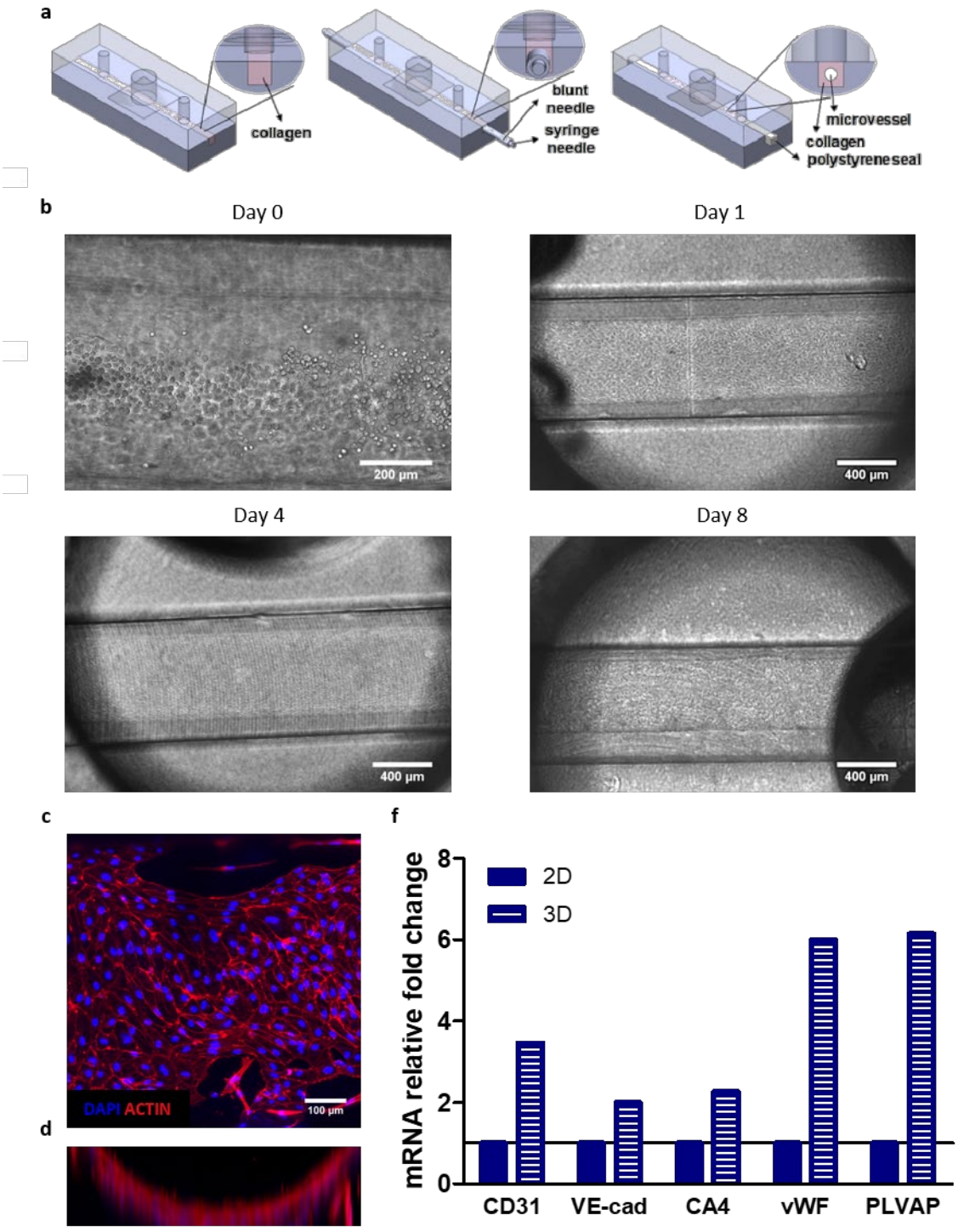

Figure 10. **hiPSC-derived EC culture in the microfluidic device. a** Schematic representation of the hydrogel patterning in the microfluidic device. **b** Microscopic images of the formation by hiPSC-derived ECs of a tubular structure at day 0, 1, 4, and 8 respectively. **c** Maximum projection of confocal image of an immunostained tubule for DAPI and actin at day 3 of culture. **d** 3D reconstruction of a confocal Z-stack showing the cross-section of the microchannel with ECs growing as a continuous monolayer leaving and empty lumen in the center. **e** Gene expression of ECs at passage 1 derived from cell line ips17-00095 cultured in 2D and in the microfluidic device. The graph shows data of three (2D), and one biological replicates (3D). Gene expression is indicated relative to hiPSC-derived ECs cultured in 2D at passage 1.

Culturing of hiPSC-derived RPE on-a-chip. For modeling of the retinal epithelium, hiPSC-derived RPE was cultured on the open-top chamber of the microfluidic device. HiPSC-derived RPE were seeded on a synthetic membrane with irregular pore distribution as a means of mimicking the BrM. Since hiPSC-

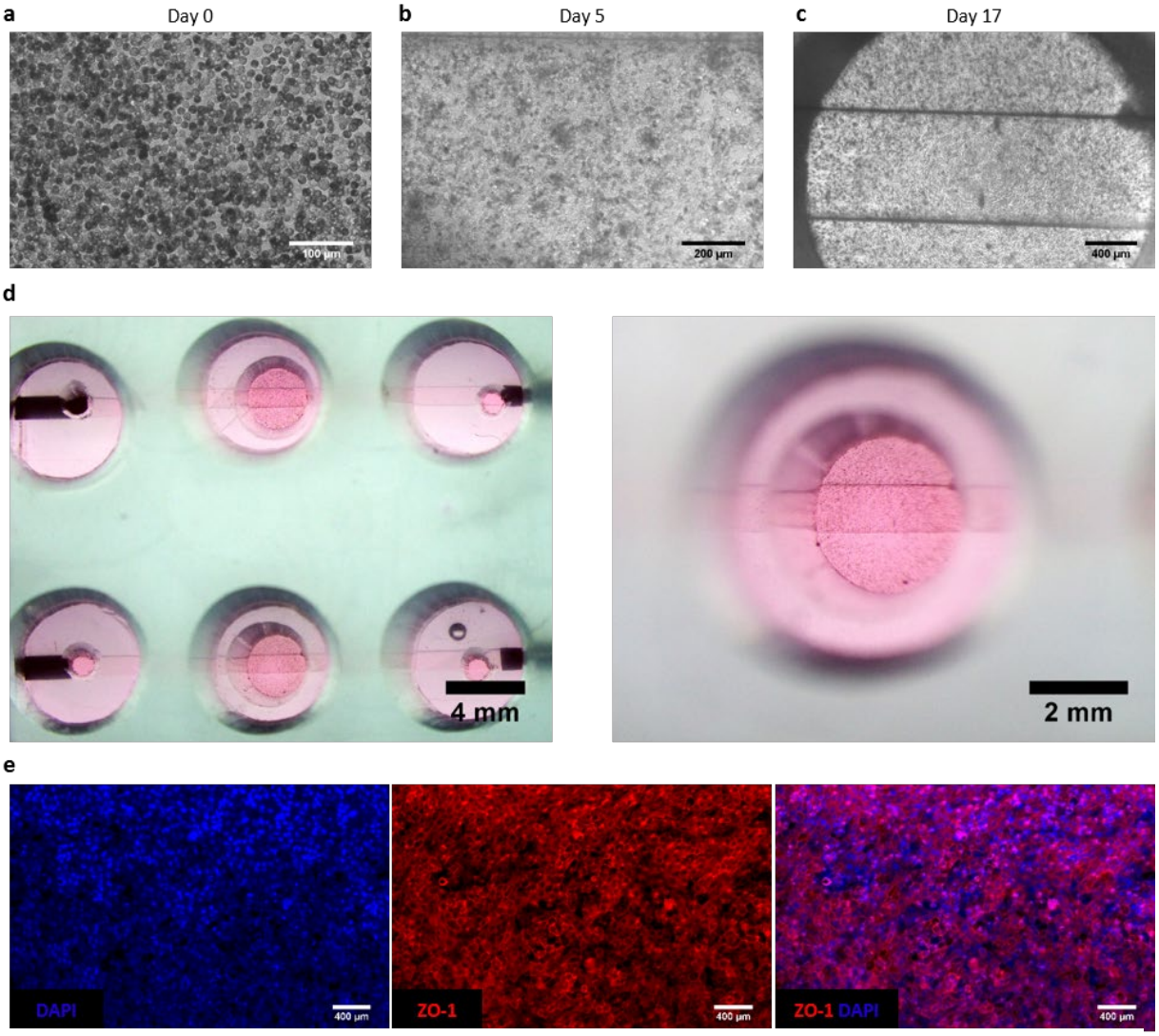

Figure 11. **hiPSC-derived RPE culture in the microfluidic device. (a-c)** Microscopic images of the hiPSC-derived RPE development at day 0, 5, and 17 respectively. **a** hiPSC-derived RPE at passage 1 were seeded with $4{,}5{\cdot}10^4$ cells per chamber. **b** hiPSC-derived RPE were confluent with cobblestone morphology after 5 days of culture. **c** hiPSC-derived RPE were fully confluent and mature at day 17 of culture. **d** Pigmentation was visual by the naked eye at day 17 of culture. **e** Maximum projections of microscopic images of ZO-1 immunohistochemistry staining in the microfluidic device at day 17 of culture

derived RPE proliferate very slowly, high cell density was needed to achieve a confluent and pigmented monolayer within a short time span (**Figure 11a**). The monolayer was fully confluent in 5 days with typical RPE hexagonal shape (**Figure 11b**). After 12 more days in culture, pigmentation was distinguishable by the naked eye, indicative of a mature monolayer (**Figure 11c-d**). The culture remained viable for more than 3 weeks (data not shown). **Figure 11d** also shows that the surface area of the open upper chamber is much larger than that of the microfluidic channel reducing the area of contact between the endothelial tubule and the epithelium. Lastly, the hiPSC-derived RPE were immunoreactive to ZO-1, indicating that the cells formed a tight cellular barrier on the microfluidic device (**Figure 11e**).

Development of hiPSC-derived RPE and ECs co-culture on-a-chip. Once the two cell types were optimized separately, they were incorporated in the microfluidic device at different time points. First, the hiPSC-derived RPE were seeded on the open-top chamber and allowed to proliferate forming a confluent and mature monolayer. Then, by day 17, the hiPSC-derived ECs were seeded on the microchannel flowing the standard protocol. **Figure 12a** depicts a cross-section of the hiPSC-derived RPE

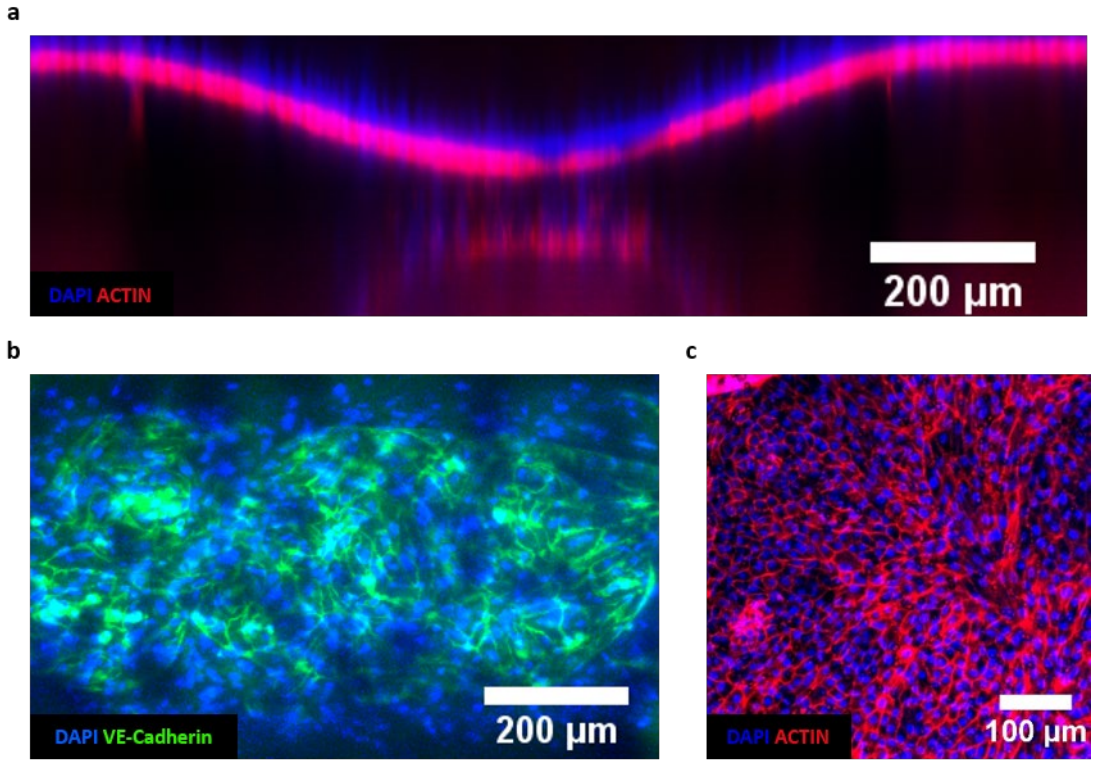

Figure 12. **hiPSC-derived RPE and ECs co-culture in the microfluidic device. a** 3D reconstruction of a confocal Z-stack showing the cross-section of the hiPSC-derived RPE and ECs co-culture DAPI-actin staining at day 19 of culture. **b** Maximum projection of a confocal image of an immunostained hiPSC-derived endothelial tubule for VE-cadherin EC-specific marker in co-culture with hiPSC-derived RPE. **c** Maximum projection of a confocal image of a DAPI-actin stained hiPSC-derived RPE monolayer in co-culture with hiPSC-derived ECs.

and EC co-culture, showing that the ECs are contained within the collagen lumen and the RPE form a continuous monolayer atop the channel. hiPSC-derived ECs in co-culture with hiPSC-derived RPE express the endothelial specific surface marker as shown by immunofluorescence staining for VE-cadherin (**Figure 12b**). The medium chosen for the co-culture was the EC-SFM medium, since hiPSC-derived ECs do not survive under FMN (data not shown). Culturing hiPSC-derived RPE with a different medium than its own had a negative impact on cell morphology as depicted on **Figure 12c**. To further evaluate the

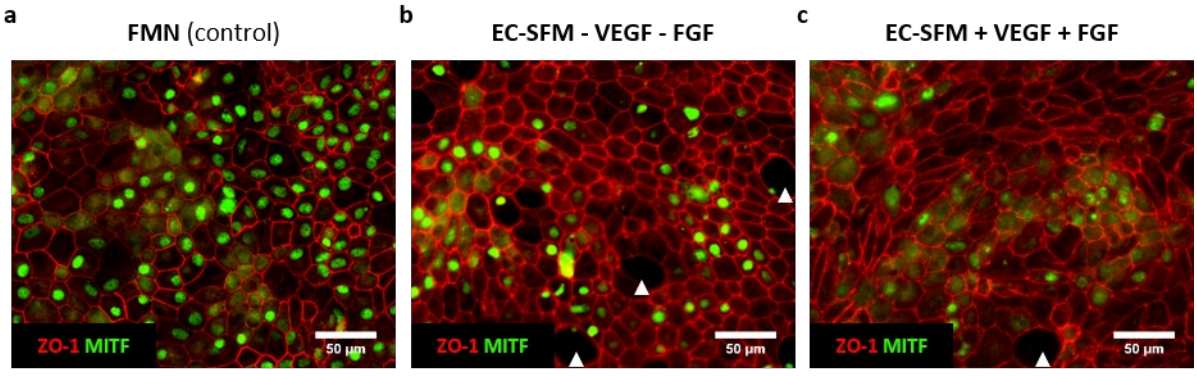

Figure 13. **Effect of medium composition on hiPSC-derived RPE. (a-c)** Maximum projections of microscopic images of ZO-1 and MITF immunohistochemistry staining when cultured for one week on **a** FMN (control), **b** EC-SFM medium composed of human endothelial serum-free medium and 1% of platelet-poor plasma-derived human serum, and **c** EC-SFM medium composed of human endothelial serum-free medium and 1% of platelet-poor plasma-derived human serum, 30 ng/ml of VEGF, and 20 ng/ml of bFGF. White arrowheads indicate the presence of holes in the epithelium.

effects of EC-SFM medium composition on hiPSC-derived RPE, ZO-1 and MITF protein expression was analyzed by immunofluorescence (**Figure 13a-c**). Once hiPSC-derived RPE were confluent, epithelial monolayers incubated for one week with EC-SFM with and without 30 ng/ml VEGF and 20 ng/ml bFGF were compared to control monolayers cultured in FMN. As expected, in the control group, ZO-1 proteins were properly organized in a hexagonal pattern (**Figure 13a**). Additionally, MITF expression was observed nearly in all the cells. In contrast to the control group, incubation of hiPSC-derived RPE monolayers with EC medium induced functional and morphological changes with a substantial redistribution of ZO-1 tight junction protein, the appearance of holes, and decreased MITF expression (**Figure 13b**). These alterations were more pronounced on the monolayers incubated with EC-SFM supplemented with VEFG and bFGF (**Figure 13c**).

Discussion

Because AMD is a heterogeneous and multifactorial ocular disease, there are no good models that can capture the intriguing complexity of the human macula's anatomy and function. First, animal models and immortalized cell lines do not consider the genetic and environmental variability amongst patients. Secondly, 2D monocultures are too simplistic models that fail to recapitulate the multilayered architecture of the oBRB. In order to understand the etiology of the disease and to develop effective treatment strategies, a model that incorporates relevant cell sources arranged in a more physiological configuration is required. This study shows that an oBRB model exclusively composed of hiPSC-derived cells cultured in an OoC device can be developed replicating the key anatomical parts of the RPE-choroid interface.

The use of hiPSC as a cell source shows great promise for acquiring a better understanding of the human physiology *in vitro*. This is of particular importance when studying the interplay between different cell types, as in the case of the RPE-choroid interface, so that all cell types carry the same genetic information. Also, they circumvent the shortcomings of ethical concerns and availability issues of other cell sources. Despite this, one critical weakness of hiPSCs is their immature phenotype and functionality, akin to their respective fetal cells[22]. One contributing factor is that cells in culture dishes are not exposed to the same mechanical and biochemical cues as they do *in vivo*. For example, while oxygen concentration in the mammalian retina varies from 0.5% to 7%, in culture conditions is maintained at 20%[23]. This great difference can alter their metabolism leading to a cell culture behavior not found *in vivo*[24]. Similarly, it was discovered that hiPSC-derived ECs had low levels of glycocalyx, vital to vascular homeostasis. By closing the mitochondrial permeability transition pore with cyclosporine-A, the glycocalyx was restored improving functional maturation (data not published). Furthermore, batch-to-batch variability and the occurrence of a heterogeneous population at the end of the differentiation protocol, impede reproducibility, and consistency in the generation of cells from hiPSCs. Our data indicate that there was variability on the gene expression levels of endothelial markers within the same cell line, demonstrating variability between distinct differentiation outcomes.

The generation of hiPSC-derived RPE is extremely inefficient and time-consuming with an efficiency of around 1% after 2 to 3 months in culture. RPE yield can be increased up to 80% in 1 to 2 months by a directed differentiation method, in which medium is supplemented with chemically defined factors[25]. Moreover, at gene expression level, *RPE65* gene was upregulated in our hiPSC line by 200-fold compared to ARPE-19, highlighting the biological relevance of the hiPSC-derived RPE over immortalized cell lines, since mutations in this gene cause severe early-onset blindness[26]. Strikingly, given that counterbalance of VEFG and PEDF is essential for maintaining choroidal homeostasis, our RT-qPCR results showed a substantial difference in the mRNA expression levels, where *PEDF* was upregulated 100-fold and *VEGF* was downregulated by 2-fold compared to HUVEC. Our ELISA results revealed a polarized VEGF secretion with a stabilized concentration of 6 ng/ml overtime. However, it was 5 times lower than the exogenous VEGF concentration used for the hiPSC-derived ECs medium maintenance. Arjamaa *et al.* demonstrated that VEGF secretion from RPE cells could be increased by exposing cells to hypoxic conditions[27]. In this way, control over VEGF secretion could be achieved.

The method used to isolate ECs from hiPSCs is based on the CD31 surface marker, which is expressed across all the ECs. It is well known that ECs display tissue heterogeneity across the human body because

they are subjected to different mechanical and biochemical stresses. Therefore, the incorporation of these niche microenvironmental cues to which only the ECs of the CC are exposed could bring them closer to their *in vivo* counterpart in terms of gene expression levels and functionality. For example, it has been identified that connective tissue growth factor is secreted both by ECs and RPE and its addition to the differentiation protocol has proven to drive hiPSC towards a choroidal phenotype[28]. Our RT-qPCR data showed elevated mRNA expression levels of *CA4, vWF,* and *PLVAP,* indicating a closer gene expression profile characteristic of fenestrated capillaries[29], whereas *CD31* and *VE-cadherin* mRNA levels remained equivalent to HUVECs. Particularly, *PLVAP* was 40 times more expressed, demonstrating that our generated ECs were more permeable than HUVEC. However, HUVECs are very distant physiologically and functionally compared to the ECs of the CC reducing the relevance of this analysis. The University of Iowa has developed an immortalized human choroid endothelial cell line which could be used as better control to prove that the generated cells possess the ECs features of the CC[30].

The development of OoC platforms that closely resembles the conditions found *in vivo* is of paramount importance for the study of physiological processes *in vitro.* The integration of mechanical and biochemical cues has been demonstrated to be advantageous in mimicking the *in vivo* microenvironment. In fact, our RT-qPCR results showed that hiPSC-derived ECs performed differently in a 3D configuration by upregulating the mRNA gene expression of all the ECs specific markers. Although a 3D vessel geometry and full ECM embedment were included in this microfluidic device, shear stress was absent, which is essential for vascular homeostasis and maturation. However, the incorporation of a flow system presents one of the main limitations of OoC devices since its implementation has proven to be cumbersome.

The material used for this OoC was PDMS because it is inexpensive, easy to use, and suitable for cell culture in terms of transparency, gas permeability, and biocompatibility. However, PDMS also faces some limitations. Since the chips are handmade, there is large chip-to-chip variability, and its throughput is low, which limits experimental replicates and restrains parallelization. Also, most often these devices are not compatible with conventional microscopes, plate readers, transepithelial electrical resistance measurement machines, etc. Secondly, the fabrication method used with oxygen plasma treatment and PDMS/Toluene mortar has proven to be incapable of meeting the demands of long-term culture since medium leakage was a recurrent problem. Lastly, chemical functionalization with APTES and GA was used to immobilize collagen on PDMS. However, collagen collapse and detachment were usually observed probably due to protein dissociation from the PDMS.

The co-culture of hiPSC-derived RPE and ECs on the microfluidic device was accomplished with success, although the life span and proliferation rate of the two cell types were very different. While hiPSC-derived RPE could be cultured for more than 3 weeks in the OoC device being fully matured after 17 days, the hiPSC-derived ECs were only able to be maintained for 10 days. The procedure to achieve the co-culture of the two cell types was by seeding hiPSC-derived ECs around day 17 on a pre-patterned device, but at this timepoint the collagen condition was not optimal for hiPSC-derived ECs seeding. It has been demonstrated that hiPSC-derived ECs maintain endothelial morphology in this 3D microenvironment and express VE-cadherin differentiation marker in co-culture with hiPSC-derived RPE. However, morphological changes were observed in the hiPSC-derived RPE in co-culture since the medium used was that of the ECs. For OoC models consisting of multiple cell types, media compatibility remains a challenge with detrimental consequences on cell behavior and barrier function. Our data shows that hiPSC-derived RPE undergoes morphological changes and decreased expression of MITF

under the influence of ECs medium. These results are in alignment with other studies that have demonstrated a decreased permeability of RPE cells upon VEGF exposure, and RPE were capable of transdifferentiating into other cell types of the neural retina under the induction of bFGF[31,32].

Limitations of the model

There are some limitations of this model that should be addressed. As mentioned before, there are no mechanical cues implemented on the ECs compartment. This reduces its significance since ECs are under a constant mechanically active environment. Secondly, the distance between the endothelial tubule and the RPE monolayer is around 250 µm, considering the polyester membrane and top of the patterned hydrogel. In addition, the diameter of the endothelial tubule measures 500 µm which exceeds typical dimensions of a capillary vessel. Not only there are shortcomings of the model in terms of anatomical and physiological relevancy compared to the human environment, but also there are technical limitations that hinder the development of this OoC model. For example, the thickness of the device is much greater than the working distance of common objectives impeding the imaging of the complete system and the autofluorescence of the synthetic membrane lowers image quality. Overall, the success rate from chip manufacturing until endpoint experiment is very low, only about 30% of the devices could be used for data-gathering. This is mainly due to medium leakage, hydrogel patterning collapse, and contamination. This poses a major limitation to study prolonged molecular processes such as drusen formation on-a-chip, one of the key features to understand AMD pathology.

Improvements and future perspectives

Future work could focus on addressing the current limitations of this OoC model without any chip design modifications. To tackle the issue of static culture, a simple way to implement pump-free perfusion *in vitro* is by placing the devices in a rocker platform. This would provide continuous bidirectional flow across the device for better modeling of blood vessel physiology. Nonetheless, it would not be physiological for the RPE cells. Next, the distance between the ECs and the RPE culture chambers could be reduced by incorporating the ECs together with the hydrogel, similar to the approach developed by Peak *et al.*[19] In this way, the separation between the two compartments would correspond to the 10 µm thickness of the polyester membrane, and in turn, the endothelial cells would develop into a capillary network. Although this method would be easier to implement than the hydrogel patterning, the number of branches and the network diameter would be difficult to control. Furthermore, it is well known that mural cells, *e.g.*, pericytes, smooth muscle cells, and fibroblasts, help stabilize the vascular network by depositing local ECM[33]. With the current ECs differentiation protocol, pericytes can be derived from the CD31-negative population[21]. Thus, culturing pericytes together with ECs could be a straightforward implementation as an attempt to improve maturity and long-term stability of the vascular network.

To overcome the technical limitations, injection molding could be used as a fabrication method where the width of the device could be minimized and in turn, leakage problems could be eliminated. Also, the polyester membrane could be substituted by an optically transparent membrane derived from native ECM proteins allowing microscopic imaging and providing a more physiologically relevant context[34]. Lastly, long-term culture on microfluidic devices remains a challenge, limiting the study of drusen formation on-a-chip. Therefore, research should focus on the study of molecular processes with shorter lifespan such as proteins involved in lipid metabolism and transport. For example, lipid storage in the

cell requires the expression of lipid droplets proteins such as Fatty Acid Transport Protein 1(FATP1) and the study of its expression pattern could help predict lipid accumulation earlier[35].

Conclusion

In summary, an oBRB barrier model combining the hiPSC and OoC technology is presented. In this model, hiPSC-derived RPE and ECs are arranged in a more physiological architecture modeling the key features of the RPE-choroid interface. This work provides the basis for further development of the model, in which patient-derived cell lines from different genetic backgrounds could be used for the identification of new biomarkers and therapeutic agents to treat AMD patients paving the way towards precision medicine. Moreover, hiPSCs provide a cell source free from ethical issues, and OoC technology embraces the 3Rs guiding principles of reduction, refinement, and replacement of animal experiments.

Acknowledgements

First of all, I would like to thank Giuliana Gagliardi and Yusuf Arık for their daily support and valuable guidance in this learning process. I am thankful to Anneke den Hollander and Andries van der Meer for giving me the chance to partake in this exciting project.

Last but not least, I also must thank Tatiana Eufrásio and Frank Walboomers from the dentist department at Radboudumc for letting me use their facility. Without them, the transfer of the device fabrication would not have been possible.

References

1. Pennington, K. L. & DeAngelis, M. M. Epidemiology of age-related macular degeneration (AMD): associations with cardiovascular disease phenotypes and lipid factors. *Eye Vis.* **3**, 1–20 (2016).

2. Friedman DS1, O'Colmain BJ, Muñoz B, Tomany SC, McCarty C, de Jong PT, Nemesure B, Mitchell P, K. J. E. D. P. R. G. Prevalence of Age-Related Macular Degeneration in the United States. **122**, (2014).

3. Mehta, S. Age-Related Macular Degeneration. *Prim. Care - Clin. Off. Pract.* **42**, 377–391 (2015).

4. Wong, T. *et al.* The Natural History and Prognosis of Neovascular Age-Related Macular Degeneration. A Systematic Review of the Literature and Meta-analysis. *Ophthalmology* **115**, 116–127 (2008).

5. A.C., B. Therapeutic targets in age-related macular disease. *J. Clin. Invest.* **120**, 3033–3041 (2010).

6. Strauss, O. The retinal pigment epithelium in visual function. *Physiol. Rev.* **85**, 845–881 (2005).

7. Lutty, G. A. *et al.* Development of the human choriocapillaris. *Eye* **24**, 408–415 (2010).

8. Booij, J. C., Baas, D. C., Beisekeeva, J., Gorgels, T. G. M. F. & Bergen, A. A. B. The dynamic nature of Bruch's membrane. *Prog. Retin. Eye Res.* **29**, 1–18 (2010).

9. Ambati, J. & Fowler, B. J. Mechanisms of age-related macular degeneration. *Neuron* **75**, 26–39 (2012).

10. Rattner, A. & Nathans, J. Macular degeneration: Recent advances and therapeutic opportunities. *Nat. Rev. Neurosci.* **7**, 860–872 (2006).

11. Galloway, C. A. *et al.* Drusen in patient-derived hiPSC-RPE models of macular dystrophies. *Proc. Natl. Acad. Sci.* **114**, E8214–E8223 (2017).

12. Zeiss, C. J. Review paper: Animals as models of age-related macular degeneration: An imperfect measure of the truth. *Vet. Pathol.* **47**, 396–413 (2010).

13. Cao, J. *et al.* A subretinal matrigel rat choroidal neovascularization (CNV) model and inhibition of CNV and associated Inflammation and fibrosis by VEGF Trap. *Investig. Ophthalmol. Vis. Sci.* **51**, 6009–6017 (2010).

14. Huh, D. *et al.* Reconstituting organ-level lung functions on a chip. *Science (80-.).* **328**, 1662–1668 (2010).

15. Trietsch, S. J. *et al.* Membrane-free culture and real-time barrier integrity assessment of perfused intestinal epithelium tubes. *Nat. Commun.* **8**, 1–7 (2017).

16. Vormann, M. K. *et al.* Nephrotoxicity and Kidney Transport Assessment on 3D Perfused Proximal Tubules. *AAPS J.* **20**, 90 (2018).

17. Chen, L. J. *et al.* Microfluidic co-cultures of retinal pigment epithelial cells and vascular endothelial cells to investigate choroidal angiogenesis. *Sci. Rep.* **7**, 1–9 (2017).

18. Chung, M. *et al.* Wet-AMD on a Chip: Modeling Outer Blood-Retinal Barrier In Vitro. *Adv. Healthc. Mater.* **7**, 1–7 (2018).

19. Paek, J. *et al.* Microphysiological Engineering of Self-Assembled and Perfusable Microvascular

Beds for the Production of Vascularized Three-Dimensional Human Microtissues. *ACS Nano* (2019). doi:10.1021/acsnano.9b00686

20. Reichman, S. *et al.* From confluent human iPS cells to self-forming neural retina and retinal pigmented epithelium. *Proc. Natl. Acad. Sci.* **111**, 8518–8523 (2014).

21. Orlova, V. V. *et al.* Generation, expansion and functional analysis of endothelial cells and pericytes derived from human pluripotent stem cells. *Nat. Protoc.* **9**, 1514–1531 (2014).

22. Karanika, S., Karantanos, T., Li, L., Corn, P. G. & Timothy, C. Current Challenges of iPSC-Based Disease Modeling and Therapeutic Implications. *Cells* **34**, 2815–2822 (2015).

23. Yu, D. Y. & Cringle, S. J. Oxygen distribution in the mouse retina. *Investig. Ophthalmol. Vis. Sci.* **47**, 1109–1112 (2006).

24. Baranov, P. Y., Tucker, B. A. & Young, M. J. Low-oxygen culture conditions extend the multipotent properties of human retinal progenitor cells. *Tissue Eng. - Part A* **20**, 1465–1475 (2014).

25. Buchholz, D. E. *et al.* Rapid and Efficient Directed Differentiation of Human Pluripotent Stem Cells Into Retinal Pigmented Epithelium. *Stem Cells Transl. Med.* **2**, 384–393 (2013).

26. Cai, X., Conley, S. M. & Naash, M. I. RPE65: Role in the visual cycle, human retinal disease, and gene therapy. *Ophthalmic Genet.* **30**, 57–62 (2009).

27. Arjamaa, O. *et al.* Hypoxia and inflammation in the release of VEGF and interleukins from human retinal pigment epithelial cells. *Graefe's Arch. Clin. Exp. Ophthalmol.* **255**, 1757–1762 (2017).

28. Songstad, E. et. al. Connective Tissue Growth Factor Promotes Efficient Generation of Human Induced Pluripotent Stem Cell- Derived Choroidal Endothelium. *Stem Cells Transl. Med.* 274-283dd (2013). doi:10.5966/sctm.2012-0084

29. Wilson, K. et. al. Concise Review: Tissue-Specific Microvascular Endothelial Cells Derived from Human Pluripotent Stem Cells. *Stem Cells* **23**, 1–7 (2008).

30. Giacalone, J. C. *et al.* Generation of an immortalized human choroid endothelial cell line (iChEC-1) using an endothelial cell specific promoter. *Microvasc. Res.* **123**, 50–57 (2019).

31. Ablonczy, Z. et. al. VEGF Modulation of Retinal Pigment Epithelium Resistance. *Natl. Inst. Heal.* **85**, 762–771 (2008).

32. Fuhrmann, S., Zou, C. & Levine, E. M. Retinal pigment epithelium development , plasticity , and tissue homeostasis. *Exp. Eye Res.* 1–10 (2013). doi:10.1016/j.exer.2013.09.003

33. Jain, R. K. RegulaçãO Molecular Da Angiogenesis. **9**, 1–9 (2003).

34. Mondrinos, M. J., Yi, Y., Wu, N., Ding, X. & Huh, D. Lab on a Chip semipermeable , optically transparent , and culture †. *Lab Chip* (2017). doi:10.1039/C7LC00317J

35. Van Den Brink, D. M. *et al.* Physiological and pathological roles of FATP-mediated lipid droplets in Drosophila and mice retina. *PLoS Genet.* **14**, 1–25 (2018).

36. The angiogenesis Foundation. The science of AMD. Available at: http://www.scienceofamd.org/learn/.

Supplementary data

Table 1. TaqMan probe assay ID list

Gene name	TaqMan probe assay ID
MERTK	Hs01031973_m1
BEST1	Hs00188249_m1
RPE65	Hs01071462_m1
PEDF (SERPINF1)	Hs01106934_m1
VEGF A	Hs00900055_m1
MITF	Hs01117294_m1
18S	Hs99999901_s1
PECAM1(CD31)	Hs00169777_m1
PLVAP	Hs00229941_m1
CA4	Hs00426343_m1
CDH5 (VE-cadherin)	Hs00901465_m1
vWF	Hs01109446_m1